Journal of Power Sources 270 (2014) 526–535

Contents lists available at ScienceDirect

Journal of Power Sources

journal homepage: www.elsevier.com/locate/jpowsour

High energy and power density asymmetric supercapacitors using electrospun cobalt oxide nanowire anode

Baiju Vidyadharan [a], Radhiyah Abd Aziz [a], Izan Izwan Misnon [a], Gopinathan M. Anil Kumar [b], Jamil Ismail [a], Mashitah M. Yusoff [a], Rajan Jose [a, *]

[a] Nanostructured Renewable Energy Materials Laboratory, Faculty of Industrial Sciences & Technology, Universiti Malaysia Pahang, 26300 Kuantan, Malaysia
[b] R&D Center, Noritake Co Ltd, 300 Higashiyama, Miyoshi, Aichi 470-0293, Japan

HIGHLIGHTS

- Asymmetric supercapacitors were fabricated with electrospun Co_3O_4 nanowires and activated carbon.
- Exhibited six fold higher energy density compared to commercial EDLC with no lowering of power density.
- Showed good cycling behaviour with ~97% retention in C_s at the end of 2000 cycles.

GRAPHICAL ABSTRACT

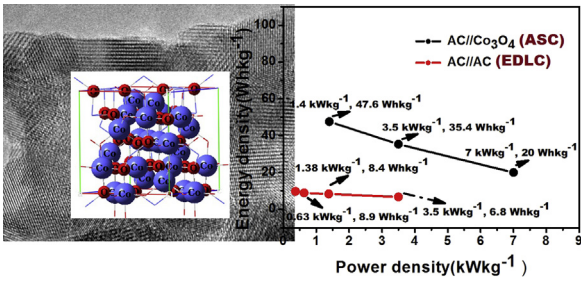

ARTICLE INFO

Article history:
Received 23 June 2014
Received in revised form
20 July 2014
Accepted 21 July 2014
Available online 28 July 2014

Keywords:
Electrochemical energy storage
Hybrid capacitors
Renewable energy
Metal oxide semiconductors
Batteries
One dimensional nanostructures

ABSTRACT

Electrochemical materials are under rigorous search for building advanced energy storage devices. Herein, supercapacitive properties of highly crystalline and ultrathin cobalt oxide (Co_3O_4) nanowires (diameter ~30–60 nm) synthesized using an aqueous polymeric solution based electrospinning process are reported. These nanowire electrodes show a specific capacitance (C_S) of ~1110 F g^{-1} in 6 M KOH at a current density of 1 A g^{-1} with coulombic efficiency ~100%. Asymmetric supercapacitors (ASCs) (C_S ~175 F g^{-1} at 2 A g^{-1} galvanostatic cycling) are fabricated using the Co_3O_4 as anode and commercial activated carbon (AC) as cathode and compared their performance with symmetric electrochemical double layer capacitors (EDLCs) fabricated using AC (C_S ~31 F g^{-1} at 2 A g^{-1} galvanostatic cycling). The Co_3O_4//AC ASCs deliver specific energy densities (E_S) of 47.6, 35.4, 20 and 8 Wh kg^{-1} at specific power densities (P_S) 1392, 3500, 7000 and 7400 W kg^{-1}, respectively. The performance of ASCs is much superior to the control EDLCs, which deliver E_S of 9.2, 8.9, 8.4 and 6.8 Wh kg^{-1} at P_S 358, 695, 1400 and 3500 W kg^{-1}, respectively. The ASCs show nearly six times higher energy density (~47.6 Wh kg^{-1}) than EDLC (8.4 Wh kg^{-1}) without compromising its power density (~1400 W kg^{-1}) at similar galvanostatic cycling conditions (2 A g^{-1}).

1. Introduction

Energy storage devices are increasingly popular nowadays due to wide popularity of multifunctional hand-held electronic devices and hybrid/plug-in electric vehicles [1]. Secondary lithium ion

* Corresponding author.
E-mail addresses: rjose@ump.edu.my, joserajan@gmail.com (R. Jose).

http://dx.doi.org/10.1016/j.jpowsour.2014.07.134
0378-7753/

batteries (LIB) and supercapacitors (SCs) are two popular protocols for energy storage devices because they are rechargeable, could be produced in diverse design with light weight and flexibility, and are easy to manufacture. The LIB provides high energy density (E_S ~150–200 Wh kg^{-1}) but at the expense of cycle life (<10^3 cycles) and power density (P_S ~0.5–1 kW kg^{-1}); whereas SCs have higher P_S (2–10 kW kg^{-1}) and longer cycle life (10^4–10^6 cycles) but their E_S is much lower (<5 Wh kg^{-1}) [2–6]. Supercapacitors are of two types based on the energy storage mechanism, viz. (i) electrochemical double layer capacitors (EDLCs) in which a non-faradic charge accumulation occurs at a porous electrode–electrolyte interface; and (ii) pseudocapacitors (PCs), which is based on a faradic reaction at the electrode–electrolyte interface. Allotropes and polymorphs of carbon are choice to build commercial EDLCs whereas PCs are built from ceramic nanostructures and conducting polymers. Recent reviews on supercapacitors are published elsewhere [5,7–9]. Commercial EDLCs suffer from lower E_S which prevent them from large scale industrial applications. Therefore, unifying high E_S and P_S in SCs is an elusive issue.

The E_S and P_S are related through.

$$\left.\begin{aligned} E_S &= \frac{1}{2} C_S V^2; \\ P_S &= \frac{Es}{\Delta t} \end{aligned}\right\} \quad (1)$$

where C_S is the specific capacitance, V is the maximum achievable voltage, and Δt is the discharge time of a SC. According to Eq. (1), there are two ways to enhance the E_S. One way is to use novel electrode material with high C_S, such as PC materials and the other is to broaden the cell voltage. Therefore, materials that offer higher C_S and V are preferred as a SC electrode for high E_S and P_S.

A high specific surface area of the electrode material to enable a large electrode–electrolyte interface for efficient redox reaction, high electrical conductivity to enable high rate charging and discharging, and availability of a range of energy states in the host material are the properties of a material to be selected as electrode in PCs. Although PCs have up to 100 times higher C_S than that of EDLCs their cycle life are relatively lower (<10^4) because charge transfer process between the electrode–electrolyte interface in the former is relatively irreversible than the charge accumulation at the interface in the later [10]. Owing to its desirable electrochemical properties for delivering high C_S, cobalt oxide (Co_3O_4) gained considerable attention as a PC electrode [11–16]. Theoretically Co_3O_4 would deliver C_S of ~3560 F g^{-1}, considering its redox potential (ΔE) at ~0.5 V, which is much higher than that of widely studied hydrated ruthenium oxide ($RuO_2 \cdot nH_2O$) (~2200 F g^{-1}) and MnO_2 (~1360 F g^{-1}) [13,17]. Many efforts are made to optimize Co_3O_4 morphologies and it's composite with carbon structures/metal to enable high C_S and cycling stability [16]; a summary of which is in Table 1. The C_S of Co_3O_4 nanoparticles are much lower [18,19], typically <10% of the theoretical value, except the hydrothermally grown ones [20]. Although addition of graphene or carbon nanotubes could enhance the conductive properties of the electrode [21] a composite of these carbon structures with Co_3O_4 also did not improve the C_S of the resulting electrodes [22–24]. Table 1 clearly shows that one-dimensional (1D) morphologies and flowers of Co_3O_4 show remarkably higher C_S [14,15,17].

The improved electrochemical performances of the electrodes using 1D structures are expected to arise from anisotropic charge transport properties; and therefore, they are of considerable importance as PC electrodes and LIB [25]. Among the many techniques for forming 1D morphologies, electrospinning is a simple and versatile technique for producing 1D nanostructures and membranes for many engineering applications including filtration, healthcare, and energy [26,27]. In the electrospinning technique, an organic polymeric solution injected through a syringe needle is spun by an electric field (~10^5 V m^{-1}) and is collected on a surface. However, evaporation of large volume of organic solvents during electrospinning have adverse environmental effects; this drawback could be removed by greener processes employing aqueous polymeric solutions.

For a given pseudocapacitive electrode, the V could be widened by choosing an electrolyte with much different electrochemical potential than the electrode material [11,28,29]. Operating cell voltage as high as 2.7 V is achieved by organic electrolytes and 3.5 V by ionic liquids [30]. However, high cost and toxicity, low conductivity, flammability, and stringent device fabrication requirements in air free atmosphere prevent them from using in large scales. Otherwise, aqueous electrolytes are environmentally benign and easy to handle but suffer from narrow operation voltage window (<1 V; theoretical stability window 1.23 V) [31]. This drawback could be eliminated by fabricating hybrid or asymmetric supercapacitors (ASCs) by combining a PC anode and an EDLC cathode

Table 1
Summary of research describing the electrochemical properties of the Co_3O_4 electrode.

Morphology	Method of synthesis	C_S (F g^{-1})	C_S retention (cycles)	Current density	Electrolyte	Ref.
Co_3O_4 nanowire	Ammonia exploration	922	95% (5000)	2 A g^{-1}	1 M KOH	[15]
Ultra layered	Homogeneous precipitation	548	99% (2000)	8 A g^{-1}	1 M KOH	[12]
Co_3O_4/graphene Nanosheets	Ultra sonication	341	89% (1000)	10 mV s^{-1}	6 M KOH	[23]
Net like Co_3O_4	Solvothermal	1063	91% (1000)	10 mA cm^{-2}	6 M KOH	[53]
rGO/Co_3O_4	One step hydrothermal	263	92% (1000)	0.2 A g^{-1}	2 M KOH	[24]
Hollow Co_3O_4 boxes	Re-crystallization	278		0.5 A g^{-1}	3% KOH	[54]
MWCNT/Co_3O_4		200.9			1 M KOH	[22]
Co_3O_4 nanoparticles	Hydrothermal	928	93% (3000)	1.2 A g^{-1}	2 M KOH	[20]
Co_3O_4/graphene	In situ solution	478		5 mV s^{-1}	2 M KOH	[55]
Co_3O_4 nanoparticle	Microwave assisted	519	99 (1000)	0.5 A g^{-1}	2 M KOH	[18]
Nanoforest	Cathodic co deposition	2.04 F cm^{-2}	84% (1500)	5 mV s^{-1}	2 M KOH	[56]
Porous Co_3O_4	Solid state thermolysis	150	100% (3400)	1 A g^{-1}	2 M KOH	[57]
Co_3O_4 nanotubes	template	574	95% (1000)	0.1 A g^{-1}	6 M KOH	[58]
Nanoplate/graphite sheet	Two step method	337.8	93% (1000)	0.2 A g^{-1}	6 M KOH	[59]
Co_3O_4 nanowire	Reflux method	336	98% (400)	1 A g^{-1}	6 M KOH	[60]
Graphene nanosheets/Co_3O_4	Microwave assisted method	243.2	96% (2000)	10 mV s^{-1}	6 M KOH	[16]
Hollow nanowires	Hydrothermal	599	91% (7500)	2 A g^{-1}	1 M KOH	[14]
Thin film	Spray pyrolysis	74	100% (1000)	5 mV s^{-1}	2 M KOH	[61]
Nano flower	Solvothermal	1936	78% (100)	0.2 A g^{-1}	6 M KOH	[17]
Nanoparticles	Plasma spray	162	72% (1000)	2.75 A g^{-1}	6 M KOH	[19]
Co_3O_4 nanowire	Electrospinning	1110	98% (2000)	1 A g^{-1}	6 M KOH	This work

[32]. As a result, operation voltage could be increased even in aqueous electrolytes thereby increasing the E_S significantly.

Considering all the above factors, ultrafine nanowires of Co_3O_4 were developed using an aqueous polymeric solution based electrospinning process and examined its suitability as a PC electrode. The electrospun Co_3O_4 electrodes showed C_S as high as 32% of its theoretical value with desirable charge–discharge cycling performance. Asymmetric supercapacitors fabricated using these electrodes as anode and commercial activated carbon (AC) as cathode gave the highest E_S so far achieved in these types of devices without compromising the P_S. The performance of the present ASC is six times higher than a control device, which is a symmetric EDLC, fabricated using AC. The ASCs could be cycled over 2000 times in the voltage range 0–1.4 V with minimal (~3%) capacity fading. To our knowledge, this is the first time such high performance devices are realized in simple device structures.

2. Experimental details

2.1. Synthesis and characterization of Co_3O_4 nanowires

A previously reported electrospinning procedure [33] was used to synthesize the Co_3O_4 nanowires with modifications. In contrast to the previous work [33] that involved multistep solution preparation procedure and intermediate heating stages, the procedure adopted in this work was simple and straightforward in which the solution was prepared in a single step without any heating procedure. Starting materials for the present work were cobalt acetate tetrahydrate [$Co(CH_3COO)_2 \cdot 4H_2O$; CoAc; 99%; Sigma Aldrich, USA] and polyvinyl alcohol (PVA; Mw – 95,000, Merck). In a typical synthesis, CoAc (0.9 g) was dissolved in 15 ml aqueous PVA solution (7 wt.% PVA in water), which gave ~0.24 M solution, and stirred for 20 h at room temperature to form a homogeneous solution. The solution was electrospun using a commercial electrospinning unit (Electroris, nanoLab, Malaysia) with a solution injection rate of 0.5 ml h^{-1} using a 21G needle and at a potential of ~24 kV. The solid fibres were collected at a distance of ~17 cm away from the spinneret. The relative humidity of the electrospinning chamber was maintained at ~30%. The as-spun fibres were calcined at 500 °C for 1 h in air to remove the polymeric components and to allow nucleation and growth of Co_3O_4.

Crystal structure of the material was studied by X-ray diffraction (XRD) technique using Rigaku Miniflex II X-ray diffractometer employing CuKα radiation ($\lambda = 1.5406$ Å). Morphology of the materials was studied by scanning electron microscopic technique (7800F, FESEM, JEOL, USA). High resolution lattice images and selected area diffraction patterns were obtained using transmission electron microscope (HRTEM) operating at 200 kV (FEI, Tecnai G_2). The BET surface area of the material was measured using gas adsorption studies employing a Micromeritics (Tristar 3000, USA) instrument in the nitrogen atmosphere.

2.2. Electrode preparation and electrochemical tests

It is imperative to understand the properties of the PC and EDLC electrodes separately for fabrication ASCs with optimum performance. First we studied the electrochemical properties of the single PC and EDLC electrodes in three-electrode configuration. Next, the electrochemical properties ASCs were studied in two-electrode configuration.

The electrodes were fabricated on pre-cleaned nickel foam substrates. The nickel foam was cleaned by degreasing in acetone, etching in 1 M HCl for 15 min, and subsequently washing in water and ethanol for 5 min each. Required amounts of the active materials (Co_3O_4 nanowires/activated carbon) were separately mixed with polyvinylidenefluoride (PVDF) (Sigma Aldrich, USA) and carbon black (Super P conductive, Alfa Aesar, UK) in the ratio 75:10:15. The above mixture was stirred in *N*-methyl-2-pyrrolidinone for better homogeneity. The as-prepared slurry was then pasted on the cleaned nickel foam substrate (area ~1 cm^2) and dried in an oven at 60 °C for 24 h. The dried electrode was then pressed using a hydraulic press at a pressure of 5 ton.

Electrochemical properties of each electrode were studied by cyclic voltammetry (CV), galvanostatic charge–discharge cycling (CDC), and electrochemical impedance spectroscopy (EIS) in 6 M KOH electrolyte in three-electrode configuration. Mass loading of the Co_3O_4 and AC was ~2.0–2.5 mg and ~3.0–4.0 mg, respectively. A potentiostat–galvanostat (PGSTAT M101, Metrohm Autolab B.V., The Netherlands) employing NOVA 1.9 software was employed for electrochemical tests. A platinum rod and a saturated Ag/AgCl electrode were used as the counter and the reference electrodes, respectively. The ASCs were fabricated by assembling the Co_3O_4 nanowire and the AC electrodes as anode and cathode separated by a glass microfiber filter (fioroni) in 6 M KOH. The amount of active materials for fabrication of ASC was calculated from the C_S determined from CDC curves in the three-electrode configuration.

3. Result and discussion

Although aqueous polymeric solution based electrospinning is reported for synthesis of Co_3O_4 nanowires by Barakat et al. [33] the diameters of the wires were ~450 nm, which are much higher for an improved performance in a device. In this work, the precursor concentration is optimized for getting nanowires of diameter 1/10th of that reported before (Fig. 1). The solution was optimized

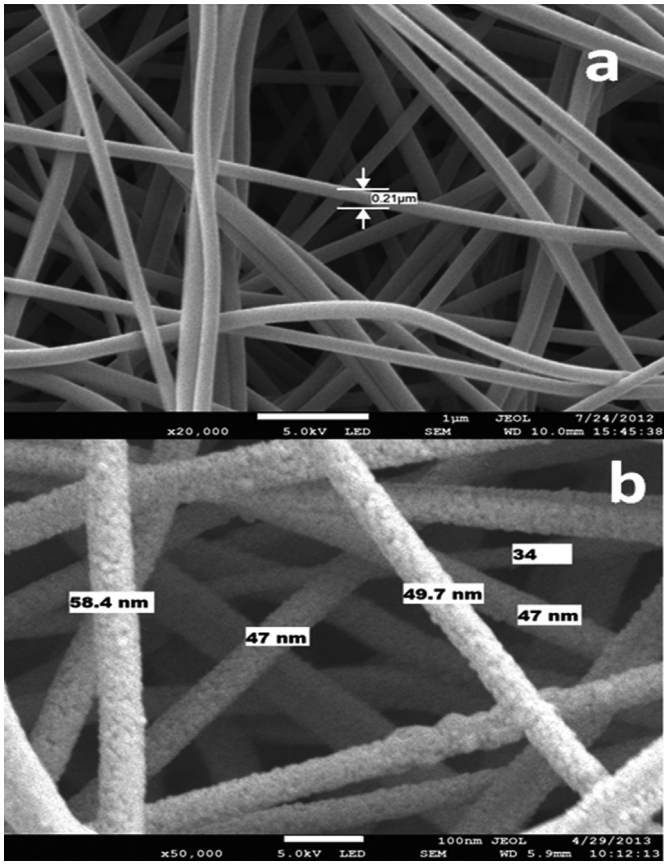

Fig. 1. The FESEM images of (a) as-prepared polymeric nanofibers and (b) calcined Co_3O_4 nanowires.

(0.24 M) for getting the lowest diameter of the final ceramic; any solution lower concentrated than 0.24 M did not yield wires whereas the higher ones increased the diameter >100 nm (See Supplementary information S1).

3.1. Morphology, crystal structure, and surface properties of electrospun Co_3O_4 nanowires

A thorough characterization of the morphology and crystal structure of the annealed electrospun materials has been undertaken. Morphological and structural details of the Co_3O_4 nanowires are summarized in Figs. 1 and 2 (More figures are in Supplementary information S1 & S2). The as-prepared wires are uniform and had an average diameter of ~250 nm, which upon annealing reduced to ~30–60 nm. The bright field TEM image in Fig. 2(a and b) shows that the fibres are made of particles of size ~2–10 nm with dense packing. The particles are of well faceted cuboidal morphology with sharp edges (Fig. 2(b)). A selected area diffraction pattern (SAED) of a typical nanowire segment is in Fig. 2(c). The SAED pattern consists of diffraction spots oriented in typical polycrystalline ring patterns which further confirm the high degree of particle orientation in the nanowires. The SAED pattern is indexed for a face centred cubic (space group: $Fd\bar{3}m:2$) structure with lattice constant $a = 8.0732$ Å. A high resolution lattice image of a typical particle is shown in Fig. 2(d); well-ordered lattice fringes are clearly visible in HRTEM images thereby indicating that the nanowires are well crystallized. The particles are observed to be free from crystal defects such as line and point defects; therefore, they could be called as "highly crystalline". The XRD pattern of the Co_3O_4 nanowires showed diffraction peaks (Fig. 3) correspond to the $Fd\bar{3}m:2$ space group; the lattice parameter obtained from the diffraction pattern is $a = 8.0561$ Å, the value matches very well with that reported for Co_3O_4 (PDF card No. 653103) and that determined from SAED patterns [34]. All these characterizations confirm that the single phase nanowires of Co_3O_4 are obtained through the electrospinning procedure.

The measured BET surface area of the Co_3O_4 nanowires was ~13.6 $m^2\ g^{-1}$ with a pore volume of ~0.5 $cm^3\ g^{-1}$, which are at lower end for wires of diameter ~30–60 nm. The observed relatively lower surface area is partly contributed by dense particle packing in the wires that reduced porosity despite the lower wire diameter. The Barrett–Joyner–Halenda (BJH) analysis showed a mean pore size of ~11.2 nm because the dense particle packing resulted in larger pores (See the TEM images in the Supporting information S2). The observed mean pore size is higher than the size of solvated ions in typical aqueous electrolytes such as KOH (size of K^+ ~3.31 Å), which is used in this work for electrochemical evaluation (Section 3.2), which would reduce the kinetic charge transfer resistance at the electrode–electrolyte interface and would increase the achievable capacitance [35].

3.2. Electrochemical properties of Co_3O_4 nanowires electrode

Prior to discussing the properties of the final ASCs, it is imperative to understand the electrochemical properties of the components electrodes, i.e., the anode formed of the Co_3O_4 nanowires and cathode from the commercial AC (surface area ~1820 $m^2\ g^{-1}$). Typically, properties of a single electrode are

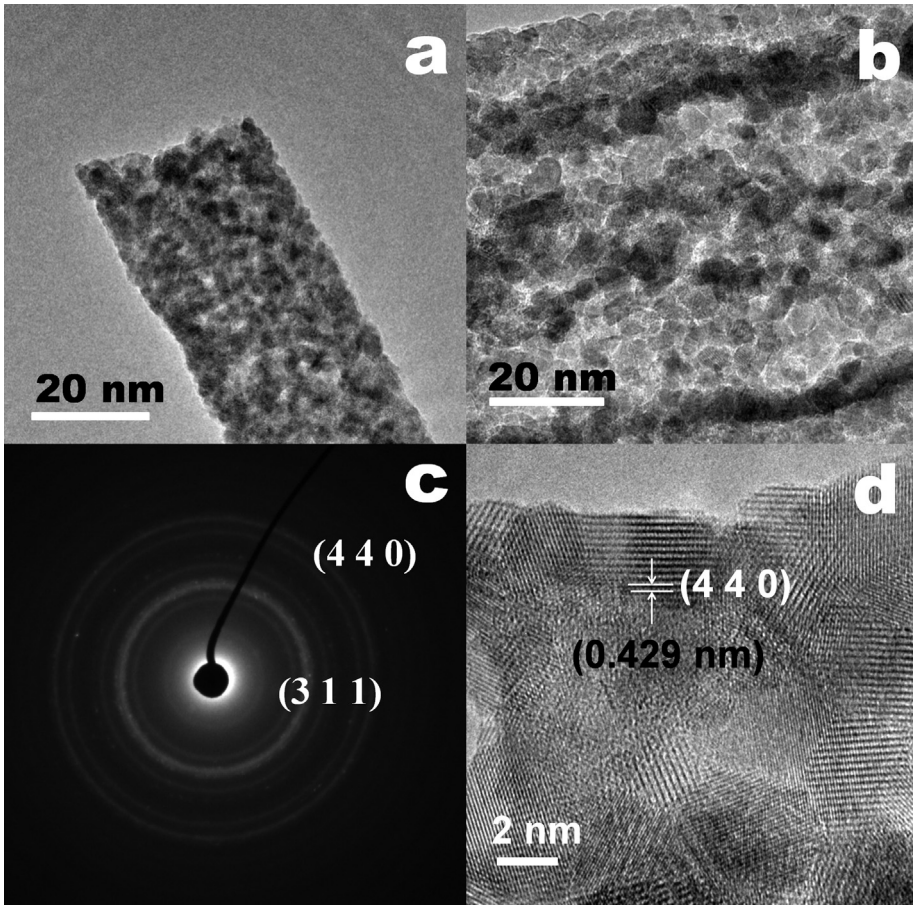

Fig. 2. (a & b) Bright field image of a typical nanowire; (c) selected area electron diffraction pattern; (d) high resolution lattice image of a typical particle in the TEM sample.

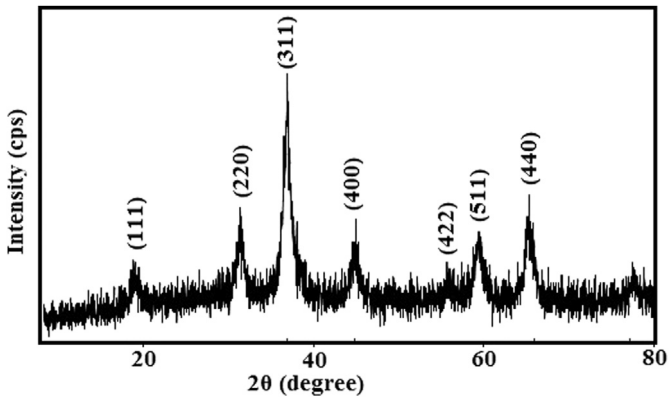

Fig. 3. The XRD pattern of cobalt oxide nanowires.

characterized by a three-electrode configuration consisting of the working electrode, reference electrode, and counter electrode. The CV curves of the Co_3O_4 nanowires measured in 6 M KOH aqueous solution in the voltage window 0–0.5 V at different scan rates between 2 and 50 mV s^{-1} is in Fig. 4(a). The CV profiles show oxidation (anodic) and reduction (cathodic) events, which are characteristics of PCs. The anodic peak in the CV profile shifted towards positive potentials with increase in the scan rate and the cathodic peak to the negative potential on account of the polarization in the electrode material. The asymmetric and scan rate dependent shape of the CV profile show that the origin of the capacitance is by the faradic reaction. Redox peaks are observed at all scan rates, which corresponds to the conversion between different oxidation/reduction states of cobalt according to the reaction [36–41],

$$Co_3O_4 + 4H_2O + 2e^- \underset{\text{Discharging/oxidation}}{\overset{\text{Charging/reduction}}{\rightleftharpoons}} 3Co(OH)_2 + 2OH^-$$

$$3CoOOH + e^- \underset{\text{Discharging}}{\overset{\text{Charging}}{\rightleftharpoons}} Co_3O_4 + OH^- + H_2O$$

The C_S was estimated from the CV using the relation.

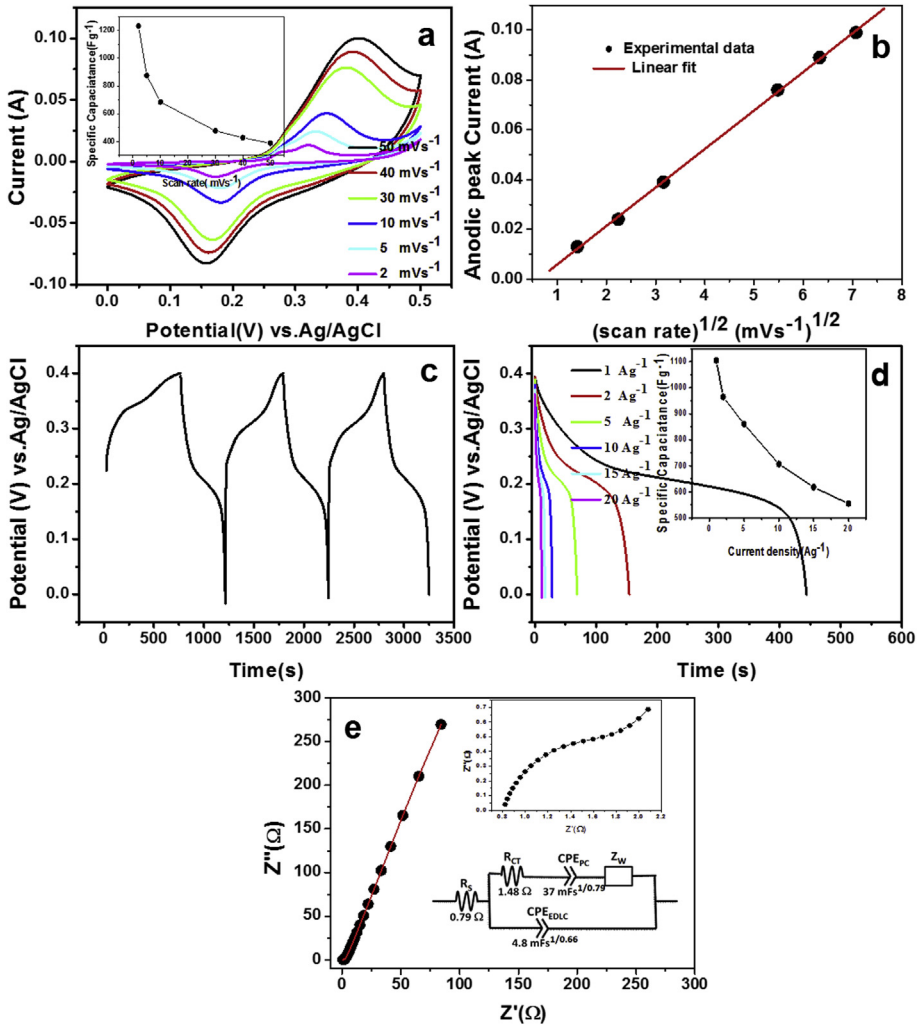

Fig. 4. (a)The CV data of the Co_3O_4 nanowire electrode in 6 M KOH aqueous solution at scan rates between 2 and 50 mV s^{-1} with respect to Ag/AgCl reference electrode; (inset) variation in C_S with scan rate; (b) anodic peak current versus square root of scan rate indicating bulk diffusion of ions during the electrochemical reaction; (c) The first three charge–discharge curves of the Co_3O_4 nanowire electrode in 6 M KOH aqueous solution at a galvanostatic current density of 1 A g^{-1}; (d) The discharge curves of the Co_3O_4 nanowire electrode at different current densities in 6 M KOH aqueous solution; (inset) variation of specific capacitance of nanowire electrode calculated from discharge curves; (e) Nyquist plot for Co_3O_4 nanowire electrode at open circuit potential; the solid circle indicates are experimental values and the continuous line is the fitted data. The insets show the expanded high frequency region and electrical equivalent of the pseudocapacitor electrode showing the transport parameters.

$$C_S = \frac{1}{mv(E_2 - E_1)} \int_{E_1}^{E_2} i(E)dE \quad (2)$$

where E_1 and E_2 are the cutoff potentials in the CV curves and $i(E)$ is the current at each potential, E_2–E_1 is the potential window, m is the mass of the active material, and v is the scan rate. The calculated C_S from the CV curves is in the inset of Fig. 4(a). While comparing with the theoretical C_P of Co_3O_4 (~3560 Fg^{-1}), the observed C_S (1080 Fg^{-1}) at 2 mV s^{-1} is ~30%, which leads us to conclude that a majority of the available surface of the active material in the electrode contributed to the electrochemical reaction. Slower scan rates enable higher diffusion of ions into the Co_3O_4 nanowires thereby accessing a major fraction of the active site in the material and show high C_S. In pseudocapacitive materials, such as Co_3O_4, the scan rate (v) dependence of voltammetric current (i) is analysed to determine whether the capacitance originates from surface redox reaction or from bulk diffusion. The $i \propto v$ for surface redox reaction and $i \propto \sqrt{v}$ for semi-infinite bulk diffusion [2]. A straight line for $i \propto \sqrt{v}$ (Fig. 4(b)) is observed; therefore, bulk diffusion occurred during the electrochemical reaction, which is expected to be the source of the observed high capacitance.

To isolate the supercapacitive performance of the Co_3O_4 nanowires from the Ni foam substrate, the background capacitance of Ni foam was evaluated from the area under the CV curve. The area of the CV curve without using the Co_3O_4 nanowires was ~1.3×10^{-4}, which is only ~0.01% of the total area in the presence of it (See Supporting information, S3), thereby suggesting that contribution from the Ni foam is negligible in our experiment.

The pseudocapacitive performance of the Co_3O_4 nanowire electrodes were evaluated from the galvanostatic charge–discharge curves in the voltage range of 0–0.4 V in 6 M KOH electrolyte. The first three charge discharge curves of the Co_3O_4 nanowire electrode at a galvanostatic current density of 1 Ag^{-1} in 6 M KOH is in Fig. 4(c). The potential drop during the discharge process, generally caused by the internal resistance (R) and incomplete faradic reaction of the device, was rather low (~5 mV) indicating ideal CDC in the present Co_3O_4 nanowires [42]. This lowering of R could be attributed to the high electrical conductivity offered by less-defective particles forming the electrospun nanowires (Fig. 2) and high ionic conductivity of the 6 M KOH electrolyte used in this work.

The galvanostatic discharge curves at various current densities from which usually practically available C_S of a single electrode is calculated is in Fig. 4(d). The discharge curve is observed to be a combination of three processes, viz. (i) a fast initial potential drop followed by (ii) a slow potential decay, and (iii) a faster voltage drop corresponding to EDLC. The first two sections are assigned to oxidation $Co(OH)_2$ to Co_3O_4 as observed from the CVs. The clear non-linear shape of the discharge curves (Fig. 4(d)) and the deviation from rectangular shape of the CV (Fig. 4(a)) reveal that the major contribution of C_S of the Co_3O_4 electrode material originates from faradic reactions.

The C_S was calculated from the charge–discharge curves using the relation.

$$C_S = \frac{It}{m\Delta V} \quad (3)$$

where I, t, m and ΔV are applied current, time, active mass, and potential range of the charging and discharging events, respectively. The C_S calculated from galvanostatic discharge curves as a function of specific current density is in the inset of Fig. 4(d). The C_S decreased with increasing current density similar to that observed in the CV measurements. The total C_S has contribution from C_P and EDLC. The contribution of C_S from the substrate was also studied in 6 M KOH from the discharge curves without using the Co_3O_4 nanowires (See Supplementary information S4). The discharge time was 5 s for Ni foam alone whereas it was 443.8 s using Co_3O_4 nanowires; thereby demonstrating that capacitive contribution from the substrate could be neglected.

Similarly, the electrochemical behaviour of the AC electrode was also characterized in a three-electrode configuration (See Supplementary information S5). A C_S ~193 Fg^{-1} was calculated at 2 mV s^{-1} from CV and 187 Fg^{-1} from CDC at 1 A g^{-1}.

The EIS measurements were carried out to determine the electrode kinetics. The Nyquist plot of the Co_3O_4 nanowire electrode determined by EIS in the frequency range 100 kHz–0.01 Hz at open circuit potential (0.3 V) in 6 M KOH is in Fig. 4(e). The EIS spectra of a supercapacitor device is usually divided into three segments following three processes; (i) the bulk resistance of the device (R_S), synonymously called equivalent series resistance (ESR) at high frequency (>1 kHz); (ii) capacitive effects at intermediate frequencies (<1 kHz); and (iii) Warburg impedance resulting from the diffusion of OH^- ion within the pores of Co_3O_4 nanowires during redox reaction at the low frequencies (<5 Hz) [43,44]. The near straight line which make an angle ~25° with the imaginary axis indicate a lower diffusion resistance; and therefore, the electrode process is a combination of diffusive and capacitive. The observed high capacitance could be attributed to this lower diffusion resistance through easy accessibility of OH^- ions in the Co_3O_4 nanowire thereby increasing the redox reaction during charging and discharging. The R_S is a combination of (i) electrolyte resistance, (ii) intrinsic resistance of the electro active material, and (iii) the contact resistance between the active material and the current collector that determines the high frequency off-set of the EIS spectrum [45,46]. The value of R_S determined from the high frequency off-set of the EIS spectra is ~0.8 Ω which is at the lower ends of the values reported for Co_3O_4 based PCs. The lower value of R_S could be attributed to the high crystallinity of the present Co_3O_4 nanowires in addition to the one-dimensional morphology and ultrafine wire diameter. The diameter of the first semicircle is a measure of the kinetic resistance to ions transfer at the electrode–electrolyte interface, known as the charge transfer resistance (R_{CT}). The R_{CT} measured from the diameter is 1.42 Ω, which is in close agreement with the value reported for high performing Co_3O_4 electrodes [47,48].

The Nyquist plot is further fitted to an electrical equivalent circuit (inset of Fig. 4(e)) to determine the charge transport parameters. The high frequency offset, determining R_S, is modelled as a resistance. The EDLC and PC are modelled as parallel connected constant phase elements (CPE) because the total capacitance for parallel connection is the sum of the individual capacitances. The CPE allows modelling of a distribution of capacitances typically required for disordered surface structure similar to the present Co_3O_4 electrode. The CPE impedance (Z_{CPE}) is given by the following equation [32]:

$$Z_{CPE} = \frac{1}{B(j\omega)^n} \quad (4)$$

where B and n ($0 < n < 1$) are frequency-independent parameters. The system behave as a pure capacitor for $n = 1$ and pure resistor for $n = 0$. The ion diffusion in the electrolyte is modelled using a Warburg element. The R_{CT} is modelled as resistor in series with the Z_{CPE}. The experimental Nyquist plot is fitted to the above circuit. A best fit ($\chi^2 > 10^{-4}$) gave the following values: R_S ~0.79 Ω, R_{CT} ~ 1.48 Ω, Z_{CPE} (EDLC) ~4.9 $mFs^{(1/0.66)}$, Z_{CPE}(PC) ~37.1 $mFs^{(1/0.79)}$.

The fitted values of R_S and R_{CT} are in close agreement with that calculated empirically from the EIS data; therefore, the observed high C_S from CV and CDC experiments are reproduced by the EIS. To mention, the circuit shown in the inset of Fig. 4(e) produced the best fit among many circuits considered with varied choices of CPE and pure capacitors.

3.3. The electrochemical characterization of Co_3O_4//AC ASCs

First criterion for fabrication of ASCs is the charge balance at the cathode and anode for optimum performance because the device is equivalent to two capacitors in series [49]. The charge balance will follow the relationship, $q_+ = q_-$, where q_+ is the charge stored at the anode and q_- is that at the cathode. The charge on each electrode is given by $q = C_S \times \Delta V \times m$, [50] where ΔV is the potential window, from which the mass on the respective electrode for optimum performance is given by [49,51]

$$\frac{m+}{m-} = \frac{C_S(\mathrm{EDLC}) \times \Delta V_-}{C_S(\mathrm{PC}) \times \Delta V_+} \quad (5)$$

On the basis of the C_S values and potential windows of the Co_3O_4 nanowire and AC electrodes determined separately as explained above, the optimized mass ratio for fabrication of ASC was calculated to be 0.42. A total of four ASCs were fabricated with cathode mass-loading up to 4 mg and anode mass-loading up to 2.5 mg to confirm the consistence of the results.

A symmetric supercapacitor using the commercial AC (mass loading ~3.6 mg) is also fabricated here for comparison. The CV curves of AC//AC symmetric capacitor and the Co_3O_4//AC ASCs at different scan rates in the potential window 0–1.4 V are in Fig. 5(a & a_1), respectively. Nearly rectangular shape and scan independent shape of CV curves (Fig. 5(a)) of the symmetric capacitors shows that the capacitance originates from EDLC. The CV curves of the ASC (Fig. 5a_1) exhibited with a region of broad redox peaks

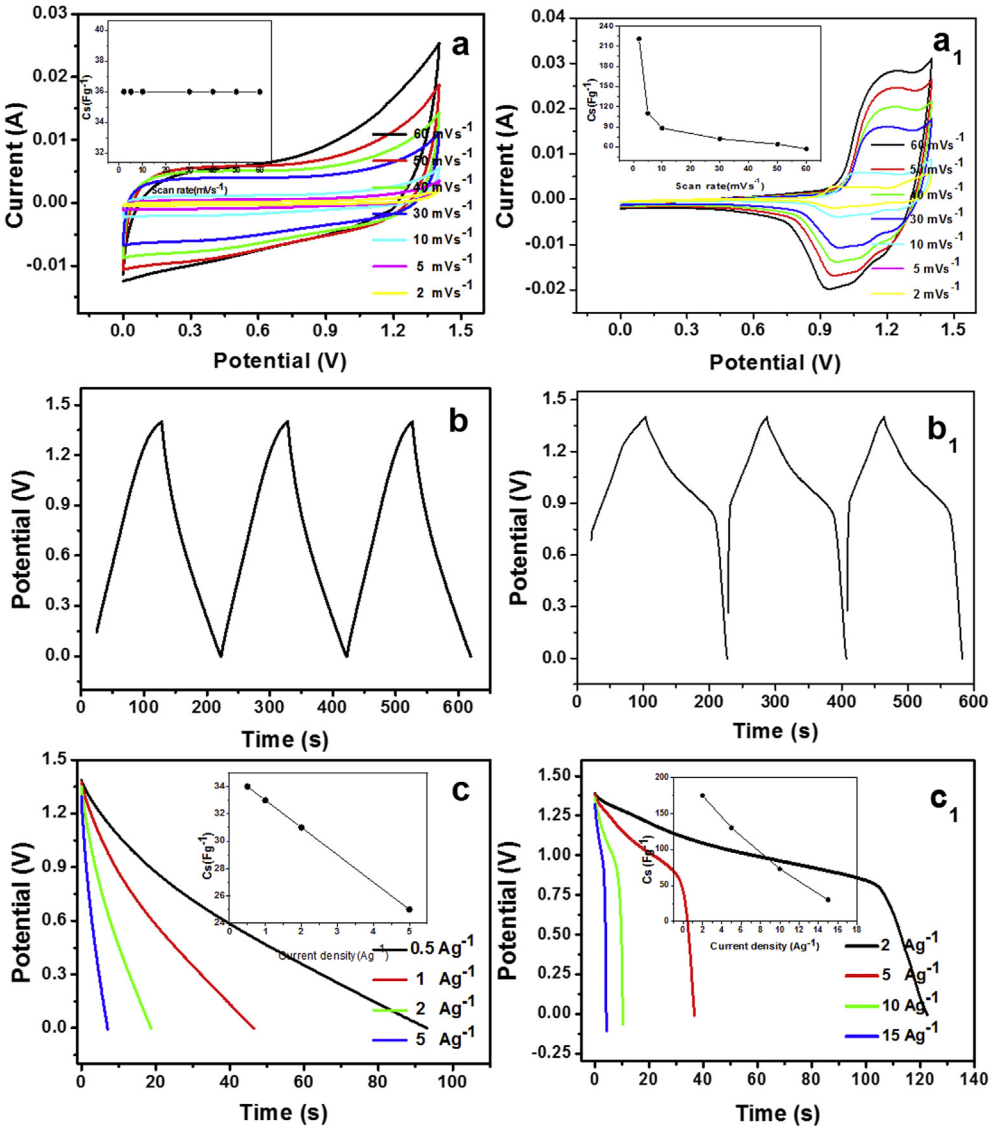

Fig. 5. (a) The CV data of the AC//AC symmetric capacitor in 6 M KOH aqueous solution at scan rates between 2 and 60 mV s^{-1};inset shows variation in C_S with scan rate; (a_1) The CV data of the Co_3O_4//AC asymmetric supercapacitor in 6 M KOH aqueous solution at scan rates between 2 and 60 mV s^{-1};inset shows variation in C_S with scan rate; (b) The first three charge–discharge curves of the AC//AC symmetric supercapacitor in 6 M KOH aqueous solution at a galvanostatic current density of 1 A g^{-1}; (b_1) The first three charge–discharge curves of the Co_3O_4//AC asymmetric capacitor in 6 M KOH aqueous solution at a galvanostatic current density of 2 A g^{-1} (c) The discharge curves of the AC//AC symmetric capacitor at different current densities in 6 M KOH aqueous solution; inset variation of specific capacitance of the device calculated from discharge curves; (c_1) The discharge curves of the Co_3O_4//AC asymmetric capacitor at different current densities in 6 M KOH aqueous solution; inset variation of specific capacitance of the device calculated from discharge curves.

characteristic of faradic pseudocapacitance and a region without any redox peaks characteristic of EDLC. The scan rate dependent behaviour of C_S explicitly shows that the electrochemical capacitance of an ASC depends on the positive electrode material. The shape of the CV curves remains same with the changes of scan rate, showing its good electrochemical performance.

To further evaluate the electrochemical performance, galvanostatic charge discharge was conducted at varying current densities. In Fig. 5(b & b_1) the first three charge discharge cycles at a current density 1 A g^{-1} of the symmetric and 2 A g^{-1} in asymmetric supercapacitors are presented. The discharge curves at different current densities are used to evaluate the rate capability and quantify C_S [Fig. 5(c & c_1)]. The inset of the respective figures shows the variation of C_S as a function of current density. The specific capacitance decreases with an increase in current density because the movements of electrolyte ions are restricted at high current densities. The maximum C_S of ASC is 175 Fg^{-1} at a discharge current density of 2 A g^{-1}.

The electrochemical stability of the device was evaluated through a cyclic charge discharge process at a current density of 5 A g^{-1} and cycling charge discharge testing at progressively increasing current densities. The ASC exhibits capacitive retention of ~97% at the end of the 2000 cycles. The coulombic efficiency of majority of points during the cycling is 99% while few points with 98% are also observed [Fig. 6(a)]. The rate capability of the device which was evaluated by CDC at various current densities 2, 5, and 10 A g^{-1} respectively is shown in Fig. 6(b). It is found that the device retains nearly the same C_S at all current densities. After continuous cycling for 1500 cycles at different current densities, the current density is brought back to 2 A g^{-1} for the last 500 cycles where the capacitance of the device found to be decreased by 2%. These retention rates at a high charge discharge conditions are comparable and even superior to those reported for AC//Co_3O_4 in 6 M KOH [52] (Table 2).

Fig. 6(c) shows the Nyquist plot of the Co_3O_4//AC and AC//AC Supercapacitors determined by EIS in the frequency range 0.01 Hz–100 kHz at open circuit potential in 6 M KOH. The value of R_S determined from the high frequency off-set of the EIS spectra is ~0.65 Ω which is desirable for high P_S.

The E_S and P_S of the ASCs were calculated using the Eq. (1) and corresponding Ragone plot is in Fig. 6(d). The ASC delivered E_S of 47.6, 35.4, 20 and 8 Wh kg^{-1} at P_S of 1392, 3500, 7000 and 7400 W kg^{-1}, respectively. On the other hand, performance of the control EDLC is much inferior. The EDLC delivered E_S of 9.2, 8.9, 8.4 and 6.8 Wh kg^{-1} at P_S 358, 695, 1400 and 3500 W kg^{-1}, respectively. Interestingly, in contrast to the conventional ASCs, in which the P_S is compromised for higher E_S, the P_S of the present ASC using Co_3O_4 nanowires is superior to that of the EDLC at all E_S. We believe that this superior behaviour is due to the directional charge storage properties of the nanowires. In short, the E_S of the Co_3O_4//AC ASC reaches 47.6 Wh kg^{-1} at a P_S of 1.4 kW kg^{-1} which is six times higher than those of symmetrical AC//AC supercapacitor (8.4 Wh kg^{-1}) at current density 2 A g^{-1}

Finally, we compare the performance of the present ASCs with other devices employed various ceramic nanostructures as anode and the AC as the cathode (Table 2). Although there are many ASCs are reported which employed a composite of ceramics with carbon nanotubes(CNT)/graphene as anode and CNT/graphene as cathodes, details of which are available in a recent review article[12], they are omitted from the present comparison for the sake of simplicity. Clearly, the present devices shows the highest E_S and P_S reported for similar type of devices. The higher E_S with high P_S could be attributed to the optimized extreme lower diameter (~30–60 nm) and their relatively higher crystallinity that resulted

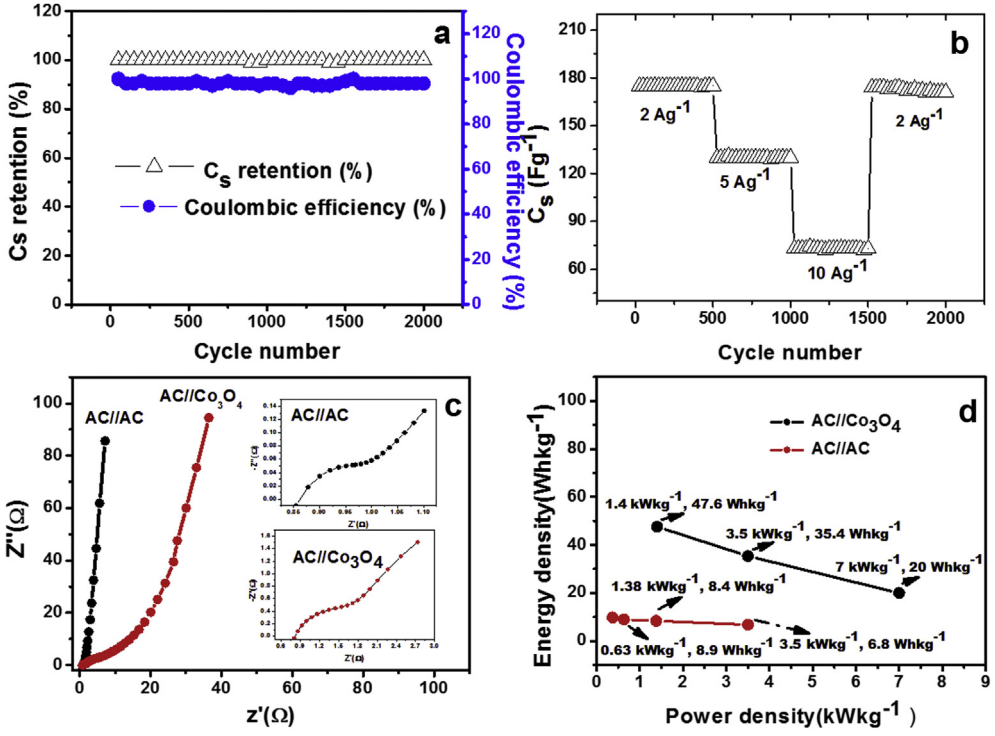

Fig. 6. (a) Dependence of the discharge C_S and the columbic efficiency as a function of charge–discharge cycle numbers. The charge–discharge tests were performed at 5 A g^{-1} in 6 M KOH aqueous solution; (b) dependence of the discharge C_S as a function of charge–discharge cycle numbers at progressively varying current densities; (c) Nyquist plot for both AC//AC and Co_3O_4//AC devices at open circuit potential. The insets show the expanded high frequency regions; (d) Comparative Ragone plots of the symmetric and asymmetric supercapacitors.

Table 2
Comparison of energy storage parameters of ASC devices employing other TMOs reported in literature with that of the present Co_3O_4//AC ASCs. GR = graphene; NR = not reported; PMT = poly(3-methyl thiophene); PPy = polypyrrole.

SC configuration	Electrolyte	C_S (F g^{-1})	Max V	E_S (Wh kg^{-1})@P_S (kW kg^{-1})	C_S retention (%)/cycle number	Ref.
$Ni(OH)_2$//AC	6 M KOH	105	1.6	36.2@0.1	92/1000	[62]
Mn_3O_4@GR//AC	6 M KOH	38	1.6	13.5@0.4	100/8000	[28]
$Ni_{0.61}Co_{0.39}$//AC	2 M KOH	130.2	1.5	36.5@0.1	62.16/1000	[63]
Co_3O_4//AC	6 M KOH	81	1.5	24.9@0.2	90/5000	[52]
Fe_3O_4//AC	6 M KOH	37	1.2	NR	82/500	[64]
Ni_3S_2//AC	2 M KOH	55.8	1.6	19.8@0.8	90/5000	[47]
$Ni_xCo_{3-x}O_4$//AC	2 M KOH	105	1.6	37.4@0.2	82.8/3000	[65]
Ni–Co–Cu oxy hydroxide//AC	1 M NaOH	58	1.8	NR	94.5/4000	[66]
$Na_{0.35}MnO_2$//AC	0.5 M Na_2SO_4	157	1.6	42.6@0.1	98/5000	[67]
Co_3O_4@NiOH//AC	6 M KOH	110.6	1.7	41.9@0.4	81/1000	[68]
α-Bi_2O_3//AC	Li_2SO_4	29	1.6	10.2@0.8	72/1000	[69]
$NiMoO_4 \cdot xH_2O$//AC	2 M KOH	96.7	1.6	34.4@0.1	80.6/1000	[70]
MnO_2–C//AC	0.5 M $NaSO_4$	56.8	2	30.6@0.2	6/5000	[71]
$Ni(OH)_2$–TH–NH_3	NR	87.8	1.6	32.7@0.071	NR	[72]
MnO_2–AC//AC	1 M Na_2SO_4	50.6	2	9.7@0.1	86/1000	[73]
CoO@PPy//AC	3 M NaOH	100	1.8	43.5@0.08	91.5/20,000	[74]
$K_{0.27}MnO_20.6H_2O$//AC	0.5 M K_2SO_4	40	1.8	25.3@0.1	100/10,000	[75]
PMT/MWNT//AC	$TEABF_4$	38.5	2.5	33.4@NR	85/1200	[76]
RuO_2/TiO_2//AC	1 M KOH	46	1.4	12.5@0.1	90/1000	[77]
Co_3O_4-rGO//AC	6 M KOH	114.1	1.5	35.7@0.2	95/1000	[78]
$NaMnO_2$//AC	Na_2SO_4	38.9	1.9	19.5@0.1	97/10,000	[79]
λ-MnO_2//AC	1 M $LiSO_4$	53	2.2	36@0.3	NR	[80]
MgO/MWCNT//AC	1 M $LiPF_6$	66	3	30@0.2	97/35,000	[81]
$Co(OH)_2$//AC	6 M KOH	38.9	1.6	13.6@0.1	86/5000	[82]
$Ni(OH)_2$/GN/NF//AC	6 M KOH	80	1.4	11.1@NR	NR	[83]
$LiMn_2O_4$//AC	1 M $LiSO_4$	NR	1.8	29.8@0.09	91/1000	[84]
α-$Ni(OH)_2$//AC	2 M KOH	127	1.2	42@0.1	82/1000	[85]
$NiCo_2O_4$//AC	1 M NaOH	NR	1.7	17.7@NR	100/2000	[86]
$NiMoO_4$-$CoMoO_4$//AC	2 M NaOH	80	1.4	28@0.1	92/1000	[87]
Co_3O_4//AC	6 M KOH	107.3	1.5	34@0.22	98/1500	[88]
Co_3O_4//AC	6 M KOH	175	1.4	47.6@1.4	97/2000	This work

in high electrical conductivity in the nanowires electrode. The Co_3O_4 based device shows 97% retention at the end of 2000 cycle which is suitable for a commercial device. Although the current device could only achieve a voltage of ~1.4 V but it is in environmentally benign and low cost aqueous KOH electrolyte. However, this drawback could be eliminated by using organic electrolytes and ionic liquids, which would deliver operating voltage window as high as ~2.7 and 3.5 V, respectively. The potential window of the present Co_3O_4 based device could be increased further by using composite anode in the same electrolyte. The high rating of the present device is expected for its success to be deployed for commercial applications.

4. Conclusions

In conclusion, conditions for forming highly crystalline ultrathin Co_3O_4 (diameter ~30–60 nm) nanowires are optimized using a "greener" electrospinning process and studied its structural, morphological, and electrochemical properties. A C_S of ~1110 Fg^{-1} in 6 M KOH at a current density of 1 A g^{-1} with coulombic efficiency ~100% is observed for the electrospun Co_3O_4 nanowires. An ASC (C_S ~175 Fg^{-1} at 2 A g^{-1} galvanostatic cycling) is fabricated using the Co_3O_4 as anode and commercial AC as cathode and compared the performance with a symmetric supercapacitor (EDLC) fabricated using AC (C_S ~31 Fg^{-1} at 2 A g^{-1} galvanostatic cycling). The ASC shows larger voltage window (V ~1.4 V) and C_S (~175 F g^{-1}) than the control device (EDLC) (V ~1.4 V; C_S ~31 F g^{-1}). The ASC delivers specific energy densities (E_S) of 47.6, 35.4, 20 and 8 Wh kg^{-1} at specific power densities (P_S) 1400, 3500, 7000 and 7400 W kg^{-1}, respectively, which is much superior to the control device. The control device delivers E_S of 9.2, 8.9, 8.4 and 6.8 Wh kg^{-1} at P_S 358, 695, 1400 and 3500 W kg^{-1}, respectively The performance of the Co_3O_4 ASCs are compared with other devices reported in literature those employed various ceramic nanostructures as anode and the AC as the cathode and found that the present nanowires show the highest E_S and P_S in devices of similar structure. In short, the ASC show nearly six times higher E_S (~47.6 Wh kg^{-1}) than SC (8.4 Wh kg^{-1}) while maintaining high P_S (~1400 W kg^{-1}) at similar galvanostatic cycling conditions (2 A g^{-1}). Because of the high rating of the present device, they could be soon be deployed for commercial applications.

Acknowledgements

This work was supported by Ministry of Higher Education (MOHE), Malaysia under Exploratory Research Grant Scheme (RDU110103) and Fundamental Research Grant Scheme (RDU 110602) on energy storage devices; and Malaysian Technological Universities Network (MTUN) grant on nanowires of metal oxide semiconductors. Research and Innovation Department, UMP is acknowledged for internal support.

Appendix A. Supplementary data

Supplementary data related to this article can be found at http://dx.doi.org/10.1016/j.jpowsour.2014.07.134.

References

[1] J. Baxter, Z. Bian, G. Chen, D. Danielson, M.S. Dresselhaus, A.G. Fedorov, T.S. Fisher, C.W. Jones, E. Maginn, U. Kortshagen, A. Manthiram, A. Nozik, D.R. Rolison, T. Sands, L. Shi, D. Sholl, Y. Wu, Energy Environ. Sci. 2 (2009) 559.
[2] I.E. Rauda, V. Augustyn, B. Dunn, S.H. Tolbert, Acc. Chem. Res. 46 (2013) 1113.
[3] A.K. Shukla, T. Prem Kumar, Wiley Interdiscip. Rev. Energy Environ. 2 (2013) 14.
[4] G. Wang, L. Zhang, J. Zhang, Chem. Soc. Rev. 41 (2012) 797.
[5] Q. Lu, J.G. Chen, J.Q. Xiao, Angew. Chem. Int. Ed. Engl. 52 (2013) 1882.
[6] J. Jiang, Y. Li, J. Liu, X.H.C. Yuan, X.W. (David) Lou, Adv. Mater. 24 (2012) 5166.

[7] M. Zhi, C. Xiang, J. Li, M. Li, N. Wu, Nanoscale 5 (2013) 72.
[8] N. Devillers, S. Jemei, M.-C. Péra, D. Bienaimé, F. Gustin, J. Power Sources 246 (2014) 596.
[9] S. Liu, S. Sun, X.-Z. You, Nanoscale 6 (2014) 2037.
[10] B.E. Conway, V. Birss, J. Wojtowicz, J. Power Sources 66 (1997) 1.
[11] F. Wang, S. Xiao, Y. Hou, C. Hu, L. Liu, Y. Wu, RSC Adv. 3 (2013) 13059.
[12] S. Meher, G. Rao, J. Phys. Chem. C 115 (2011) 15646.
[13] X.-H. Xia, J.-P. Tu, X.-L. Wang, C.-D. Gu, X.-B. Zhao, Chem. Commun. 47 (2011) 5786.
[14] X. Xia, J. Tu, Y. Mai, X. Wang, C. Gu, X. Zhao, J. Mater. Chem. 21 (2011) 9319.
[15] H. Cheng, Z.G. Lu, J.Q. Deng, C.Y. Chung, K. Zhang, Y.Y. Li, Nano Res. 3 (2010) 895.
[16] J. Yan, T. Wei, W. Qiao, B. Shao, Q. Zhao, L. Zhang, Z. Fan, Electrochim. Acta 55 (2010) 6973.
[17] X. Qing, S. Liu, K. Huang, K. Lv, Y. Yang, Z. Lu, D. Fang, X. Liang, Electrochim. Acta 56 (2011) 4985.
[18] S. Vijayakumar, A.K. Ponnalagi, S. Nagamuthu, G. Muralidharan, Electrochim. Acta 106 (2013) 500.
[19] R. Tummala, R.K. Guduru, P.S. Mohanty, J. Power Sources 209 (2012) 44.
[20] C. Yuan, L. Yang, L. Hou, L. Shen, F. Zhang, D. Li, X. Zhang, J. Mater. Chem. 21 (2011) 18183.
[21] F. Liu, C.W. Lee, J.S. Im, J. Nanomater. 2013 (2013) 1.
[22] Y. Shan, L. Gao, Mater. Chem. Phys. 103 (2007) 206.
[23] S. Park, S. Kim, Electrochim. Acta 89 (2013) 516.
[24] G.-J. Liu, L.-Q. Fan, F.-D. Yu, J.-H. Wu, L. Qiu, Z.-Y. Qiu, J. Mater. Sci. 48 (2013) 8463.
[25] M.V. Reddy, G.V.S. Rao, B.V.R. Chowdari, Chem. Rev. 113 (2013) 5364.
[26] D.H. Reneker, A.L. Yarin, Polymer 49 (2008) 2387.
[27] S. Ramakrishna, R. Jose, P.S. Archana, A.S. Nair, R. Balamurugan, J. Venugopal, W.E. Teo, J. Mater. Sci. 45 (2010) 6283.
[28] Y. Xiao, Y. Cao, Y. Gong, A. Zhang, J. Zhao, S. Fang, D. Jia, F. Li, J. Power Sources 246 (2014) 926.
[29] J. Chang, M. Jin, F. Yao, T.H. Kim, V.T. Le, H. Yue, F. Gunes, B. Li, A. Ghosh, S. Xie, Y.H. Lee, Adv. Funct. Mater. 23 (2013) 5074.
[30] L. Demarconnay, E. Raymundo-Piñero, F. Béguin, J. Power Sources 196 (2011) 580.
[31] Z. Lei, N. Christov, X.S. Zhao, Energy Environ. Sci. 4 (2011) 1866.
[32] B.E. Conway. Electrochemical Supercapacitors, Scientific Fundamentals and Technological Applications, Kluwer Acad. Publ., New York, 1997.
[33] N.A.M. Barakat, M.S. Khil, F.A. Sheikh, H.Y. Kim, J. Phys. Chem. C 112 (2008) 12225.
[34] W. Kraus, G. Nolze, J. Appl. Crystallogr. 29 (1996) 301.
[35] I.I. Misnon, R.A. Aziz, N.K.M. Zain, B. Vidhyadharan, S.G. Krishnan, R. Jose, Mater. Res. Bull. 57 (2014) 221.
[36] G. Spinolo, S. Ardizzone, S. Trasatti, J. Electroanal. Chem. 423 (1997) 49.
[37] W.K. Behl, J.E. Toni, Electroanal. Chem. Interfacial Electrochem. 31 (1971) 63.
[38] N.A. Hampson, R.J. Latham, J.B. Lee, K.I. Macdonald, Electroanal. Chem. Interfacial Electrochem. 31 (1971) 57.
[39] C. Barbero, G.A. Planes, M.C. Miras, Electrochem. Commun. 3 (2001) 113.
[40] I.G. Casella, M. Gatta, J. Electroanal. Chem. 534 (2002).
[41] X. Wang, W. Tian, C. Zhai, Y. Bando, D. Golberg, J. Mater. Chem. 22 (2012) 23310.
[42] P.S. Archana, R. Jose, C. Vijila, S. Ramakrishna, J. Phys. Chem. C 113 (2009) 21538.
[43] P. Sen, A. De, Electrochim. Acta 55 (2010) 4677.
[44] M. Ghaemi, F. Ataherian, a. Zolfaghari, S.M. Jafari, Electrochim. Acta 53 (2008) 4607.
[45] J.H. Jang, S. Han, T. Hyeon, S.M. Oh, J. Power Sources 123 (2003) 79.
[46] L. Wang, X. Liu, X. Wang, X. Yang, L. Lu, Curr. Appl. Phys. 10 (2010) 1422.
[47] C.-S. Dai, P.-Y. Chien, J.-Y. Lin, S.-W. Chou, W.-K. Wu, P.-H. Li, K.-Y. Wu, T.-W. Lin, ACS Appl. Mater. Interfaces 5 (2013) 12168.
[48] S.-W. Chou, J.-Y. Lin, J. Electrochem. Soc. 160 (2013) D178.
[49] P. Tang, Y. Zhao, C. Xu, K. Ni, J. Solid State Electrochem. 17 (2013) 1701.
[50] D. Zhang, K. Ryu, X. Liu, E. Polikarpov, J. Ly, M.E. Tompson, C. Zhou, Nano Lett. 6 (2006) 1880.
[51] P. Chen, G. Shen, Y. Shi, H. Chen, C. Zhou, ACS Nano 4 (2010) 4403.
[52] C. Zhang, L. Xie, W. Song, J. Wang, G. Sun, K. Li, J. Electroanal. Chem. 706 (2013) 1.
[53] W. Yang, Z. Gao, J. Ma, J. Wang, B. Wang, L. Liu, Electrochim. Acta 112 (2013) 378.
[54] W. Du, R. Liu, Y. Jiang, Q. Lu, Y. Fan, F. Gao, J. Power Sources 227 (2013) 101.
[55] B. Wang, Y. Wang, J. Park, H. Ahn, G. Wang, J. Alloys Compd. 509 (2011) 7778.
[56] G. Zhang, T. Wang, X. Yu, H. Zhang, H. Duan, B. Lu, Nano Energy 2 (2013) 586.
[57] F. Meng, Z. Fang, Z. Li, W. Xu, M. Wang, Y. Liu, J. Zhang, W. Wang, D. Zhao, X. Guo, J. Mater. Chem. A 1 (2013) 7235.
[58] J. Xu, L. Gao, J. Cao, W. Wang, Z. Chen, Electrochim. Acta 56 (2010) 732.
[59] L. Wang, D. Wang, J. Zhu, X. Ling, Ionics 19 (2013) 215.
[60] S.K. Meher, G.R. Rao, J. Phys. Chem. C 115 (2011) 25543.
[61] V.R. Shinde, S.B. Mahadik, T.P. Gujar, C.D. Lokhande, Appl. Surf. Sci. 252 (2006) 7487.
[62] J. Huang, P. Xu, D. Cao, X. Zhou, S. Yang, Y. Li, G. Wang, J. Power Sources 246 (2014) 371.
[63] Y. Wang, X. Zhang, C. Guo, Y. Zhao, C. Xu, H. Li, J. Mater. Chem. A 1 (2013) 13290.
[64] X. Du, C. Wang, M. Chen, Y. Jiao, J. Wang, J. Phys. Chem. C 113 (2009) 2643.
[65] X. Wang, C. Yan, A. Sumboja, P.S. Lee, Nano Energy 3 (2014) 119.
[66] C.-H. Lien, C.-C. Hu, C.-T. Hsu, D.S.-H. Wong, Electrochem. Commun. 34 (2013) 323.
[67] B.H. Zhang, Y. Liu, Z. Chang, Y.Q. Yang, Z.B. Wen, Y.P. Wu, R. Holze, J. Power Sources 253 (2014) 98.
[68] C. Tang, X. Yin, H. Gong, ACS Appl. Mater. Interfaces 5 (2013) 10574.
[69] S.T. Senthilkumar, R.K. Selvan, M. Ulaganathan, J.S. Melo, Electrochim. Acta 115 (2014) 518.
[70] M.-C. Liu, L. Kang, L.-B. Kong, C. Lu, X.-J. Ma, X.-M. Li, Y.-C. Luo, RSC Adv. 3 (2013) 6472.
[71] J.-G. Wang, Y. Yang, Z.-H. Huang, F. Kang, Carbon 61 (2013) 190.
[72] Y. Tang, Y. Liu, S. Yu, Y. Zhao, S. Mu, F. Gao, Electrochim. Acta 123 (2014) 158.
[73] X. Zhang, X. Sun, H. Zhang, D. Zhang, Y. Ma, Mater. Chem. Phys. 137 (2012) 290.
[74] C. Zhou, Y. Zhang, Y. Li, J. Liu, Nano Lett. 13 (2013) 2078.
[75] Q. Qu, L. Li, S. Tian, W. Guo, Y. Wu, R. Holze, J. Power Sources 195 (2010) 2789.
[76] P. Sivaraman, A.R. Bhattacharrya, S.P. Mishra, A.P. Thakur, K. Shashidhara, A.B. Samui, Electrochim. Acta 94 (2013) 182.
[77] Y.-G. Wang, Z.-D. Wang, Y.-Y. Xia, Electrochim. Acta 50 (2005) 5641.
[78] L.-J. Xie, J.-F. Wu, C.-M. Chen, C.-M. Zhang, L. Wan, J.-L. Wang, Q.-Q. Kong, C.-X. Lv, K.-X. Li, G.-H. Sun, J. Power Sources 242 (2013) 148.
[79] Q.T. Qu, Y. Shi, S. Tian, Y.H. Chen, Y.P. Wu, R. Holze, J. Power Sources 194 (2009) 1222.
[80] Y. Xue, Y. Chen, M.-L. Zhang, Y.-D. Yan, Mater. Lett. 62 (2008) 3884.
[81] K. Karthikeyan, S. Amaresh, V. Aravindan, Y.S. Lee, J. Mater. Chem. A 1 (2013) 4105.
[82] Y. Tang, Y. Liu, S. Yu, S. Mu, S. Xiao, Y. Zhao, F. Gao, J. Power Sources 256 (2014) 160.
[83] X. Wang, J. Liu, Y. Wang, C. Zhao, W. Zheng, Mater. Res. Bull. 52 (2014) 89.
[84] F.X. Wang, S.Y. Xiao, Y.S. Zhu, Z. Chang, C.L. Hu, Y.P. Wu, R. Holze, J. Power Sources 246 (2014) 19.
[85] J.-W. Lang, L.-B. Kong, M. Liu, Y.-C. Luo, L. Kang, J. Solid State Electrochem. 14 (2009) 1533.
[86] C.-T. Hsu, C.-C. Hu, J. Power Sources 242 (2013) 662.
[87] B. Senthilkumar, D. Meyrick, Y.-S. Lee, R.K. Selvan, RSC Adv. 3 (2013) 16542.
[88] J. Tao, N. Liu, L. Li, J. Su, Y. Gao, Nanoscale 6 (2014) 2922.